Chemical Engineering Journal 159 (2010) 1–10

Contents lists available at ScienceDirect

Chemical Engineering Journal

journal homepage: www.elsevier.com/locate/cej

Transient modeling of toluene waste gas biotreatment in a gas–liquid airlift loop reactor

Xue Wang[a,b], Xiaoqiang Jia[a,b], Jianping Wen[a,b,*]

[a] Department of Biochemical Engineering, School of Chemical Engineering and Technology, Tianjin University, Tianjin 300072, PR China
[b] Key Laboratory of Systems Bioengineering (Tianjin University), Ministry of Education, Tianjin 300072, PR China

ARTICLE INFO

Article history:
Received 27 August 2009
Received in revised form 23 January 2010
Accepted 4 February 2010

Keywords:
Toluene biotreatment
Airlift loop reactor
3D transient CFD model
Fluid hydrodynamics
Component mass transfer
Rate-limiting step

ABSTRACT

A complicated three-dimensional (3D) transient computational fluid dynamics (CFD) model was established to simulate the biotreatment of toluene waste gas in a lab scale airlift loop reactor (ALR), with multiphase flow, mass and momentum transfer and bioreaction coupled together. Multiphase flow and bioreaction were bridged by mass transfer. The model simulations were verified by the local averaged axial liquid velocities, the toluene removing efficiency (RE) and the local transient liquid phase dissolved toluene (DT). The predictions of the system shock resistance and the local transient dispersions of variables including the hydrodynamic parameters and the component concentrations were given. Furthermore, the relationship between mass transfer and bioreaction in ALR and in the draft tube were discussed quantitatively to determine the rate-limiting step. Toluene bioreaction and oxygen mass transfer are the limiting steps in the whole ALR; toluene and oxygen bioreactions are the rate-limiting steps in the draft tube. The conclusions disclose that rate-limiting step for the biotreatment process is complex and multivariate with the components and the regions in ALR.

1. Introduction

Biological purification for polluted air stream has been proved to be a cost-effective, efficient and environmentally safe way for removal of volatile organic compounds (VOCs), which are high toxic and carcinogenic pollutants threatening the environment even at low concentrations [1–4].

Biotrickling filter has been widely applied for waste gas bio-purification but has several disadvantages such as clogging problem. Since Cox et al. [5] showed rapid degradation of toluene in the recycled liquid with suspended biomass in the biotrickling filter, gas–liquid airlift loop reactor (ALR) with suspended microorganism for toluene waste gas purification is an alternative for biotrickling filter. The low energy cost and the good fluid circulation also contribute to the popularity of ALR in scientific studies and chemical industry. Although the structure of ALR is simple, the hydrodynamics, mass transfer and bioreaction in ALR are complex and they strongly couple together, making it necessary to understand the transient performance and the inner mechanism of the three aspects in the biotreatment process in ALR.

Hydrodynamics in ALR have been thoroughly studied with the aid of the CFD method. Vesvikar and Al-Dahhan [6] studied the flow pattern of ALR digester using the computational fluid dynamics (CFD) to evaluate the effect of the drift tube geometry on fluid circulation and dead volume. Roy et al. used a two-fluid CFD model to predict the flow pattern and the gas holdup in an external loop airlift reactor and good agreement was observed between the predicted and the experimental data [7]. Van Baten et al. [8] established a CFD model with Eulerian descriptions for gas–liquid flow in ALR and the model results agreed excellently with measurements.

Biotreatments of waste gas carried out in ALR have achieved satisfactory results. Wen [9] removed ethyl acetate from air streams using active sludge in an internal ALR with a removing efficiency of 98% under ethyl acetate loading of 150 mg/m^3. Livingston [10] treated 3,4-dichloroaniline (34DCA) in a similar bioreactor with a degradation efficiency of 95% and developed a steady-state biofilm kinetic model for the process to predict the rate-limiting transition from 34DCA to oxygen limitation. Lo and Hwang [11] treated toluene waste gas in ALR with the removing efficiency (RE) from 50 to 90% depending on the operating parameters and set up a regional model according to the ALR structure. The above reports have contributed to reveal the mechanism of polluted air biotreatment in ALR, but flow and bioreaction were studied separately. In fact transient flow affects oxygen and contaminant mass transfer greatly and instantaneous bioreaction directly relates to the removal effi-

* Corresponding author at: Department of Biochemical Engineering, School of Chemical Engineering and Technology, Tianjin University, Tianjin 300072, PR China. Tel.: +86 22 27890492; fax: +86 22 27402743.
E-mail address: jpwen@tju.edu.cn (J. Wen).

1385-8947/$ – see front matter © 2010 Elsevier B.V. All rights reserved.
doi:10.1016/j.cej.2010.02.006

Nomenclature

a	specific surface (m^{-1})
B	source term of bubble birth ($kg/m^3/s$)
B_{ij}	specific breakup rate of bubbles (s^{-1})
C	component concentration (kg/m^3)
C_B	constant
C_D	coefficient of drag force
C_{ij}	specific coalescence rate of bubbles (s^{-1})
C_L	coefficient of lift force
C_{VM}	coefficient of virtual mass force
C_{TD}	coefficient of turbulence dispersion force
$C_{\varepsilon 1}$, $C_{\varepsilon 2}$	coefficients in turbulence closure model
C_μ, $C_{\mu p}$	coefficients
D	source term of bubble death ($kg/m^3/s$), kinetic diffusion coefficient (m^2/s)
d	diameter (mm)
$E(\alpha_g)$	correction term
$Eö$	Eotvos number
f	size fraction of bubbles groups
f_{BV}	bubble breakup fraction
$\mathbf{g}$	gravity acceleration (m/s^2)
$\mathbf{G}_k$	turbulence birth term ($kg/m/s^3$)
h	thickness of liquid membrane (mm)
k	coefficient of mass transfer (m/s), turbulence kinetic energy (m^2/s^2)
K_i	inhibition coefficient of toluene (kg/m^3)
K_o	half-saturation coefficient of oxygen (kg/m^3)
K_s	half-saturation coefficient of toluene (kg/m^3)
$\mathbf{M}_D$	drag force (N/m^3)
$\mathbf{M}_I$	interphase force (N/m^3)
$\mathbf{M}_L$	lift force (N/m^3)
$\mathbf{M}_{TD}$	turbulent dispersion force (N/m^3)
$\mathbf{M}_{VM}$	virtual mass force (N/m^3)
m	mass (kg)
n	density of number (m^{-3})
p	pressure (Pa)
Re	Reynolds number
Re_B	bubble Reynolds number
Re_m	mixture Reynolds number
r_{ij}	equivalent radius (m)
$Rolim$	rate comparison of oxygen mass transfer and reaction
$Rtlim$	rate comparison of toluene mass transfer and reaction
S	source term of component reaction ($kg/m^3/s$)
Sc_T	turbulent Schmidt number
S_{ij}	collision square (m^2)
t	time (s)
t_{ij}	bubble coalescence time (s)
$U_{g,0}$	superficial velocity (m/s)
$\mathbf{u}$	velocity vector (m/s)
u_t	turbulent velocity (m/s)
v	bubble volume (m^3)
X	X dimension (m)
X_{jki}	mass fraction in bubble coalescence model
Y	component mass fraction
Y	Y dimension (m)
Y_{xs}	biomass yield coefficient based on substrate
Z	Z dimension (m)
Z/D	height to diameter ratio

Greek letter

α	volume fraction of phases
β	coefficient
ε	turbulent dispersion rate (m^2/s^3)
η_{ij}	collision efficiency
μ	molecular viscosity (Pa s), specific growth rate (s^{-1})
μ_{eff}	effective viscosity (Pa s)
$\mu_{g,l}$	bubble induced liquid viscosity (Pa s)
$\mu_{\max}$	maximum specific growth rate (s^{-1})
$\mu_{s,l}$	solid particle induced liquid viscosity (Pa s)
μ_T	turbulence induced viscosity (Pa s)
ρ	density (kg/m^3)
σ	surface tension (N/m)
σ_k	coefficient
σ_ε	coefficient
τ	real collision time (s)
υ	kinetic viscosity (m^2/s)
ξ	isotropic turbulence inert sub-range eddy

Superscript

*	saturation state
j	component

Subscript

0	initial state
a	algenate calium gel
g	gas phase
i	bubble size group i
j	bubble size group j
j	component
k	bubble size group k
l	liquid phase
m	mineral salt
n	nitrogen
o	oxygen
s	solid phase
t	toluene
x	biomass

ciency (RE). However, the transient waste gas biotreatment models are limited in ALR due to the complexity of the treatment process.

Since Jia et al. made a successful attempt to set up an 3D transient CFD model for phenol waste water biodegradation by immobilized cells in a pilot scale ALR [12], it is possible to establish a similar model for waste gas biotreatment in ALR.

In this paper, toluene is used as the agent for VOCs and a pure culture of strain is used for toluene biodegradation. This work aims to establish a 3D transient CFD model for the biotreatment of toluene waste gas in gas–liquid two-phase IALR to reasonably disclose the interaction of hydrodynamics and mass transfer and biodegradation in the process. The multiple size group (MUSIG) model is used to describe gas phase motion as the bubble size distribution (BSD) [13,14] theory which can provided good simulation results. The validity of the model was done by the hydrodynamic experiment and the toluene treating experiments. The inner mechanism between mass transfer and bioreaction was discussed as well as the effect of mesh partition on the simulation results, the prediction of the shock resistance and the local transient toluene and oxygen dispersions.

2. Materials and methods

2.1. Hydrodynamic experiment

The ALR used in this study is made of plexiglass, with an outer tube of 0.12 m × 0.12 m × 1.5 m, a draft tube of 0.08 m × 0.08 m × 0.8 m, and the clearance between the bottom and the drift tube of 0.02 m. The square gas distributor of 50 mm × 50 mm at the bottom has 25 holes with a diameter of 4.5 mm on it. The superficial gas velocity varies from 0.0075 to 0.02 m/s. The liquid level is 1.2 m.

Mineral salt medium is the liquid phase and air is the gas phase while the biomass concentration is set to be zero. The local liquid velocities are quantitatively measured by a backward 3D Laser Doppler Anemometer (LDA) system (DANTECH, 2017-LD 2550). LDA is a non-contact optical measurement for the liquid velocity in reactors, avoiding shortcomings of the contact methods, and has been adopted by many researchers for the airlift reactors like bubble column and ALR [15–18]. As Mudde et al. [19] and Groen et al. [20] found that the gas holdup up to 25% made the LDA system measurements credible in a two-phase bubble column, in this study the gas holdup falls in this range. The measurement for time-averaged velocity at the test point lasts for 4 min. The data is collected and processed by (FIND) software of TSI Company.

2.2. Microorganism intrinsic kinetics

Pseudomonas putida WQ-03, with a serial number of 1.1130 in China General Microbiological Culture Collection Center (CGMCCC), can use toluene as the sole carbon and energy sources and can degrade toluene thoroughly to CO_2 and H_2O according to experimental measurements. The mineral salt medium contains (mg/L): NH_4Cl: 400, KH_2PO_4: 200, $MgSO_4{\cdot}7H_2O$: 100, $FeSO_4{\cdot}7H_2O$: 20, $CaCl_2$: 20 and trace amount of $MnSO_4{\cdot}2H_2O$, $ZnSO_4{\cdot}2H_2O$, $CuSO_4{\cdot}5H_2O$, $CoCl_2{\cdot}6H_2O$ and $NaMoO_4{\cdot}2H_2O$. In batch experiments, the toluene in the headspace of the flasks is analyzed by the gas chromatography every hour until toluene could not be detected. All the experiments involved in this paper are conducted at room temperature of 25 °C, at an initial pH of 7.2 and at atmospheric pressure.

2.3. Biotreatment experiment

For toluene waste gas treatment in Fig. 1, mineral salt medium with the strain of *P. putida* WQ-03 is used as the liquid phase while air and toluene are mixed in different ratios to prepare the simulated effluent gas. The initial biomass concentration is 3.7 g/L and toluene is injected after 24-h air injection. Gas and liquid samples are taken and kept in medical syringes of 60 mL every 2 min. Gas samples were directly measured by a gas chromatography (GC9800, Kechuang) and liquid samples were centrifuged and the supernate was then measured by the same GC.

3. Model development

3.1. Model assumption

The multiphase is composed by toluene waste gas, the mineral salt medium and suspended biomass. The waste gas is the gas phase and mineral salt with suspended biomass is the liquid phase. The initial dissolved oxygen is saturated and uniformly distributed in the ALR at 25 °C. Biomass growth and toluene degradation are related to the concentrations of toluene and oxygen in the liquid phase while the impact of other medium like the mineral salts are not considered. The lag phase of the cell growth is neglected and the biomass starts form the logarithm phase. Heat transfer is not taken into account for this isothermal process.

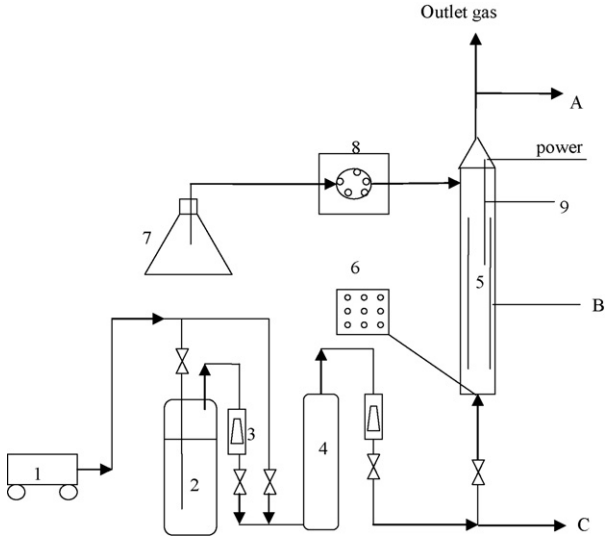

Fig. 1. Schematic diagram of the biotreatment of toluene in IALR: (1) air compressor; (2) toluene gas generating tank; (3) flow meter; (4) buffer tank; (5) IALR; (6) gas sparger; (7) mineral salt medium; (8) peristaltic pump; (9) electric heater; (A, C) gas sample points at inlet and outlet; (B) liquid sample point at 0.6 m.

3.2. Continuity and controlling equations

The continuity equations for the two phases are the same:

$$\frac{\partial(\alpha_i\rho_i)}{\partial t} + \nabla\cdot(\alpha_i\rho_i\mathbf{u}_i) = 0 \tag{1}$$

where t, α, ρ and $\mathbf{u}$ are the time, volume fraction, density and velocity of each phase, respectively. The subscript $i = g$ or l represents the gas or liquid phase and the two volume fractions sum to unity as the controlling equation.

The momentum conservation is:

$$\frac{\partial}{\partial t}(\alpha_i\rho_i\mathbf{u}_i) + \nabla\cdot(\alpha_i(\rho_i\mathbf{u}_i\mathbf{u}_i)) = -\alpha_i\nabla p + \alpha_i\rho_i\mathbf{g} + \nabla\cdot(\alpha_i\mu_{eff,i}(\nabla\mathbf{u}_i + (\nabla\mathbf{u}_i)^{\mathrm{T}})) + \mathbf{M}_I \tag{2}$$

where p is the pressure, $\mathbf{g}$ is the gravity acceleration vector and $\mu_{eff,i}$ is the effective viscosity for phase i. The term $\mathbf{M}_I$ on the right of Eq. (2) represents the interfacial forces considered in the model that determine the distribution of liquid and gas phases in the flow domain. The closure of $\mathbf{M}_I$ is described below.

3.3. Interphase forces

Interaction of dispersed and continuous phases is implemented by introducing momentum exchange terms into the respective balance equations. The interfacial forces between two phases are equal and opposite and the total interfacial forces acting on two phases include the interphase drag force, lift force, virtual mass force and turbulence dispersion force.

$$M_l = M_l^D + M_l^L + M_l^{VM} + M_l^{TD} = -M_g \tag{3}$$

The drag force is caused by the movement between the two phases [21,22]:

$$M_{lg}^D = -M_{gl}^D = \frac{3}{4}\frac{C_D}{d_m}\alpha_g\rho_l|\mathbf{u}_g - \mathbf{u}_l|(\mathbf{u}_g - \mathbf{u}_l) \tag{4}$$

where d_m is the mean bubble diameter and C_D is the drag coefficient proposed by Ishii–Zuber [23]:

$$C_D = \max\left(\frac{24}{Re_m}(1+0.15Re_m^{0.687}), \min\left(\frac{2}{3}E\ddot{o}^{1/2}E(\alpha_g), \frac{8}{3}(1-\alpha_g)^2\right)\right) \quad (5)$$

where Re_m is the mixture Reynolds number, $E\ddot{o}$ is the Eotvos number and $E(\alpha_g)$ is the correction term defined as:

$$E(\alpha_g) = \frac{1+17.67f(\alpha_g)^{6/7}}{18.67f(\alpha_g)} \quad (6)$$

$$f(\alpha_g) = \frac{\mu_l}{\mu_m}(1-\alpha_g)^{1/2} \quad (7)$$

where μ_m is the mixture viscosity.

Due to bubbles motion in the flow with shear stress, lift force acts on the direction vertical to the direction of the bubble motion:

$$M_{lg}^L = -M_{gl}^L = \alpha_g\rho_l C_L(\mathbf{u}_g - \mathbf{u}_l)\times(\nabla\times\mathbf{u}_l) \quad (8)$$

where C_L is the lift coefficient and its value is 0.5 [24,25].

Virtual mass force is caused by the acceleration of the bubbles. In this work the virtual force is mainly represented as the resistance of the liquid phase on the rising bubbles.

$$M_{lg}^{VM} = -M_{gl}^{VM} = \alpha_g\rho_l C_{VM}\left(\frac{D_g\mathbf{u}_g}{Dt} - \frac{D_l\mathbf{u}_l}{Dt}\right) \quad (9)$$

The virtual mass coefficient C_{VM} depends on shape and particle concentration and it's value for inviscid flow around an isolated spherical particle is 0.5 [26,27].

The model of Lopez de Bertodano [28] was one of the first models for the turbulent dispersion force:

$$M_l^{TD} = -M_g^{TD} = -C_{TD}\rho_l k\nabla\alpha_l \quad (10)$$

where k is the turbulence kinetic energy and the turbulent dispersion coefficient C_{TD} is between 0.1 and 1.0 for spherical particles [29] and is set to be 0.3 in this model.

3.4. Turbulence closure model

The eddy viscosity hypothesis is assumed to hold for each turbulent phase. Diffusion of momentum in each phase is governed by an effective viscosity [30]:

$$\mu_{eff,l} = \mu_l + \mu_{t,l} + \mu_{g,l} \quad (11)$$

$$\mu_{eff,g} = \mu_g + \mu_{t,g} \quad (12)$$

where μ and μ_t are the molecular viscosity and turbulence induced viscosity, respectively, while $\mu_{g,l}$ is the bubble induced viscosity of the liquid phase [31].

$$\mu_{t,l} = C_\mu\rho_l\frac{k^2}{\varepsilon} \quad (13)$$

$$\mu_{g,l} = C_{\mu p}\rho_l\alpha_g d_g|\mathbf{u}_g - \mathbf{u}_l| \quad (14)$$

where C_μ and $C_{\mu p}$ are constants and the values are 0.09 and 0.6, respectively.

The standard k–ε model presented by Launder and Spalding [32] is used to close the turbulence model.

$$\frac{\partial(\rho_l k)}{\partial t} + \nabla\cdot(\rho_l\mathbf{u}_l k) = \nabla\cdot\left[\left(\mu_l + \frac{\mu_{t,l}}{\sigma_k}\right)\nabla k\right] + \mathbf{G}_k - \rho_l\varepsilon \quad (15)$$

$$\frac{\partial(\rho_l\varepsilon)}{\partial t} + \nabla\cdot(\rho_l\mathbf{u}_l\varepsilon) = \nabla\cdot\left[\left(\mu_l + \frac{\mu_{t,l}}{\sigma_\varepsilon}\right)\nabla\varepsilon\right] + \frac{\varepsilon}{k}(C_{\varepsilon1}\mathbf{G}_k - C_{\varepsilon2}\rho_l\varepsilon) \quad (16)$$

where k is the turbulence kinetic energy and ε is the turbulence eddy dissipation. The constants are $C_{\varepsilon1} = 1.44$, $C_{\varepsilon2} = 1.92$, $\sigma_k = 1.0$ and $\sigma_\varepsilon = 1.3$. The turbulence production due to viscous forces, $\mathbf{G}_k$ is computed from:

$$\mathbf{G}_k = \mu_{t,l}\nabla\mathbf{u}_l(\nabla\mathbf{u}_l + (\nabla\mathbf{u}_l)^{\mathrm{T}}) - \frac{2}{3}\nabla\mathbf{u}_l(3\mu_{t,l}\nabla\mathbf{u}_l + \rho_l k) \quad (17)$$

3.5. Bubble size distribution theory

The dispersed gas phase is described by multiple size groups (MUSIG) model for the motion, breakup and coalescence of the bubbles. The bubble population with a diameter range of 1–15 mm is divided equally by diameter difference into 10 groups. The diameter of each bubble group is 1.7, 3.1, 4.5, 5.9, 7.3, 8.7, 10.1, 11.5, 12.9, 14.3 mm, respectively.

The population balance equation represents the continuity of particles of size v. The function $n(v,t)$ represents the number density of particles of size v at time t. Then the population balance equation is:

$$\frac{\partial(\alpha_g\rho_g f_i)}{\partial t} + \nabla\cdot(\alpha_g\rho_g u_g f_i) = S_i \quad (18)$$

$$S_i = B_{Breakup} - D_{Breakup} + B_{Coalescence} - D_{Coalescence} \quad (19)$$

where f_i is the volume fraction of size group i and S_i is the source term of mass transfer because of bubble breakup and coalescence, with two constrains:

$$\sum_1^{10} f_i = \alpha_g \quad (20)$$

$$\sum_1^{10} S_i = 0 \quad (21)$$

where $B_{Breakup}$, $D_{Breakup}$, $B_{Coalescence}$ and $D_{Coalescence}$ are the rate of birth and death of bubble breakup, birth and death of bubble coalescence, respectively.

The net source due to breakup for size group i is:

$$B_i = \alpha_g\rho_g\left(\sum_{j>i} B_{ji}f_j - f_i\sum_{j<i} B_{ij}\right) \quad (22)$$

where B_{ij} is the ratio breakup rate of size group i into size group j which sums to zero over all the groups.

$$B_{ij} = B'_{ij}\int_{f_{BV}} df_{BV} \quad (23)$$

$$f_{BV} = \frac{m_j}{m_i} \quad (24)$$

where m_i is the mass of size group i.

Luo and Svendsen [33] developed a theoretical model for the breakup of drops and bubbles in turbulent suspensions based on the theory of isotropic turbulence and probability.

$$B'_{ij} = C_B(1-\alpha_g)\left(\frac{\varepsilon}{d_i^2}\right)^{1/3}\int_{\xi_{\min}}^1 \frac{(1+\xi)^2}{\xi^{11/3}} \times \exp\left(-\frac{12(f_{BV}^{2/3} + (1-f_{BV})^{2/3} - 1)\sigma}{\beta\rho_l\varepsilon^{2/3}d_i^{5/3}\xi^{11/3}}\right) d\xi \quad (25)$$

where ξ is the dimensionless eddy size, the minimum value is:

$$\xi_{\min} = 11.4\frac{\eta}{d_i} \quad (26)$$

$$\eta = \left(\frac{1}{\varepsilon}\nu_l^3\right)^{1/4} \quad (27)$$

The value of constants used in Eq. (25) is $C_B = 0.932$, $\beta = 2$. ν_l is the liquid phase kinematic viscosity.

The net source due to coalescence for size group i is:

$$C_i = (\rho_g \alpha_g)^2 \left(\frac{1}{2} \sum_{j \le i} \sum_{k \le i} C_{jk} f_j f_k \frac{m_j + m_k}{m_j m_k} X_{jki} - \sum_j C_{ij} f_i f_j \frac{1}{m_j} \right) \quad (28)$$

where C_{ij} is the ratio coalescence rate of size group i into size group j and X_{jki} is the fraction of mass due to coalescence between groups j and k which goes into group i:

$$X_{jki} = \begin{cases} \dfrac{(m_j + m_k) - m_{i-1}}{m_i - m_{i-1}} & \text{if } m_{i-1} < m_j + m_k < m_i \\ \dfrac{m_{i+1} - (m_j + m_k)}{m_{i+1} - m_i} & \text{if } m_i < m_j + m_k < m_{i+1} \\ 0 & \text{otherwise} \end{cases} \quad (29)$$

The model of Prince and Blanch [34] assumes that the coalescence of two bubbles occurs in three steps. First, the bubbles collide with a small amount of liquid trapped between them. This liquid film then drains until it reaches a critical thickness. Then the film ruptures and the bubbles join together. The coalescence is modeled by a collision rate of two bubbles and a collision efficiency relating to the time required for the coalescence. The coalescence only due to turbulent effect is:

$$C_{ij} = \theta_{ij}^{\mathrm{T}} \eta_{ij} \quad (30)$$

The collision efficiency η_{ij} is modeled by comparing the time required for coalescence t_{ij} with the actual time during the collision τ_{ij}:

$$\eta_{ij} = \exp\left(\frac{-t_{ij}}{\tau_{ij}} \right) \quad (31)$$

$$t_{ij} = \left(\frac{\rho_l r_{ij}^3}{16\sigma} \right)^{1/2} \ln\left(\frac{h_0}{h_f} \right) \quad (32)$$

$$\tau_{ij} = \frac{r_{ij}^{2/3}}{\varepsilon^{1/3}} \quad (33)$$

where h_0 is the initial film thickness and h_f is the critical film thickness when rupture occurs, which are set to 1×10^{-4} and 1×10^{-8} mm, respectively, and r_{ij} is the equivalent radius:

$$r_{ij} = \left(\frac{1}{2} \left(\frac{1}{r_i} + \frac{1}{r_j} \right) \right)^{-1} \quad (34)$$

The turbulent contribution to collision frequency is modeled as:

$$\theta_{ij}^{\mathrm{T}} = \frac{\pi}{4} (d_i + d_j)^2 (u_{ti}^2 + u_{tj}^2)^{1/2} \quad (35)$$

where u_{ti} is the turbulent velocity given by:

$$u_{ti} = \sqrt{2} (\varepsilon d_i)^{1/3} \quad (36)$$

3.6. Component interphase mass transfer

$$\frac{\partial}{\partial t}(\alpha_g \rho_g Y_{j,g}) + \nabla \cdot (\alpha_g \rho_g \mathbf{u}_g Y_{j,g}) = \nabla \cdot \left[\alpha_g \left(\rho_g D_{j,g} + \frac{\mu_{t,g}}{Sc_{t,g}} \right) (\nabla Y_{j,g}) \right] - k_{lg}^j a_{lg} \alpha_g \rho_l (Y_{j,l}^* - Y_{j,l}) \quad (37)$$

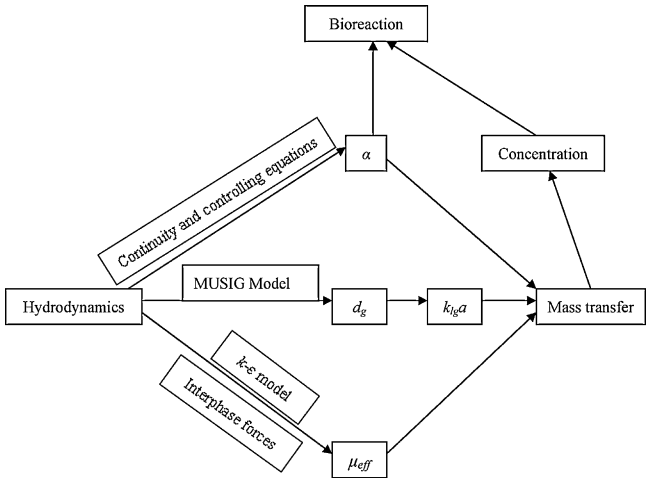

Fig. 2. Flow chart of relationship among the models of hydrodynamics, mass transfer and bioreaction.

$$\frac{\partial}{\partial t}(\alpha_l \rho_l Y_{j,l}) + \nabla \cdot (\alpha_l \rho_l \mathbf{u}_l Y_{j,l}) = \nabla \cdot \left[\alpha_l \left(\rho_l D_{j,l} + \frac{\mu_{t,l}}{Sc_{t,l}} \right) (\nabla Y_{j,l}) \right] + k_{lg}^j a_{lg} \alpha_g \rho_l (Y_{j,l}^* - Y_{j,l}) + S_j \quad (38)$$

$$\frac{\partial}{\partial t}(\alpha_l \rho_l Y_{x,l}) + \nabla \cdot (\alpha_l \rho_l \mathbf{u}_l Y_{x,l}) = S_x \quad (39)$$

where Sc is the Schmidt number, j is the component species in each phase, S is the source term of the consumption or production of the component due to the bioreaction, while $Y_{j,l}$ and $Y_{j,l}^*$ are the mass fraction of component j in the liquid phase, the saturated mass fraction of component j in the liquid phase due to their gas phase concentration, respectively; k_{lg}^j is the interphase mass transfer coefficient for component j from the gas phase to the liquid phase:

$$k_{lg}^j = 2 \left(\frac{D_{j,l}}{\pi} \right)^{0.5} \left(\frac{\varepsilon \mu_l}{\rho_l} \right)^{0.25} \quad (40)$$

where D_j is the diffusivity of species j.

3.7. Microorganism kinetic

Haldane's model is employed for toluene and Monod equation is used for oxygen. The bioreaction rate of the biomass in BC is expressed as that of Livingston [10], and Lo and Huang [11]:

$$\gamma_X = \frac{dX}{dt} = \mu_X \cdot X = \frac{\mu_{\max} S}{K_S + S + S^2/K_I} \cdot \frac{O}{K_O + O} \cdot X \quad (41)$$

where μ_X is the specific growth rate of microorganism, $\mu_{\max}$ is the maximum specific growth rate; K_S and K_O are the half-saturation constant for toluene and oxygen, X, S and O are the concentrations of biomass, toluene and oxygen in the medium, respectively; K_I is the inhibitory constant for toluene, K_O is 0.26 g/m^3 as used by Livingston [10].

The constant values of $\mu_{\max}$, K_S and K_I are obtained from batch experiments. The degradation rate of toluene is:

$$\gamma_S = \frac{dS}{dt} = \mu_S \cdot X = -\frac{\mu_X}{Y_{X/S}} \cdot X = -\frac{1}{Y_{X/S}} \frac{dX}{dt} \quad (42)$$

Integrate Eq. (42) to get the yield coefficient $Y_{X/S} = 0.57$.

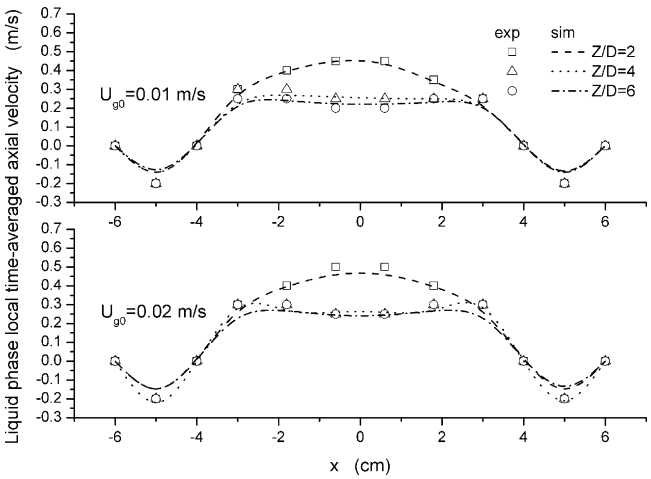

Fig. 3. Local time-averaged axial velocity from experiments and simulations.

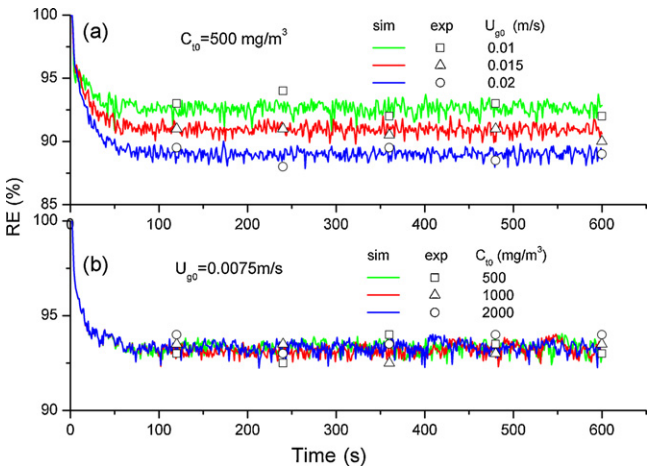

Fig. 5. (a and b) Profiles of the simulated transient results and the experimental data of RE.

The biomass specific growth rate is:

$$\mu = \frac{\mu_{\max} S}{K_S + S + S^2/K_I} \tag{43}$$

The value of $\mu_{\max}$, K_S and K_I were got from the curve fitting of μ and S. The values are 0.28 h^{-1}, 9.6 g/m^3 and 31.4 g/m^3, respectively. The bioreaction is written with biomass defined by Bailey and Ollis [35]:

$$C_7H_8 + 6.88O_2 + 0.41NH_3 \rightarrow 2.05CH_{1.84}O_{0.55}N_{0.2}(\text{biomass}) + 4.95CO_2 + 2.73H_2O \tag{44}$$

The oxygen reaction rate can be calculated by:

$$\gamma_O = 2.39\gamma_S \tag{45}$$

Fig. 2 showed how hydrodynamics, mass transfer and bioreaction were coupled together by several key parameters including the volume fraction α, the mean bubble diameter d_g, the effective viscosity μ_{eff}, the concentration and the volumetric mass transfer coefficient $k_{lg}a$.

3.8. Initial and boundary conditions

The boundary condition for the walls is defined as no-slip for the liquid phase and free-slip for the solid and the gas phases. The domain outlet is defined to allow gas to leave the domain only. In the flow simulation the mineral salt medium is the liquid phase and the treatment simulation the mineral salt medium added the biomass is used as the liquid phase.

The bubble diameter at the inlet is 8.7 mm which is the diameter of the sixth bubble group, calculating from the following equation [36]:

$$d_b = 2.9\left(\frac{\sigma d_o}{g\rho_l}\right)^{1/3} \tag{46}$$

as in this study $(d_o^{1.5} U_{g0} \rho_l \mathbf{g}^{0.5}/\sigma) \leq 1$, where d_o is the orifice diameter.

3.9. Numerical solution

The partial and ordinary differential equations described above are numerically solved in a coupled multigrid solver based on a finite volume scheme implemented in the commercial CFD code CFX, by the high resolution discretization which enable the blend factor values vary throughout the domain based on the local solution field to enforce a boundedness criterion [37]. The meshed domain with a total number of 14.520 unstructured grids of 10 mm × 10 mm × 10 mm, 15 mm × 10 mm × 10 mm and 15 mm × 15 mm × 10 mm is selected after considering both computational accuracy and the time required compared with a finer mesh of 27,000 cells. The time strategy used is the same as that

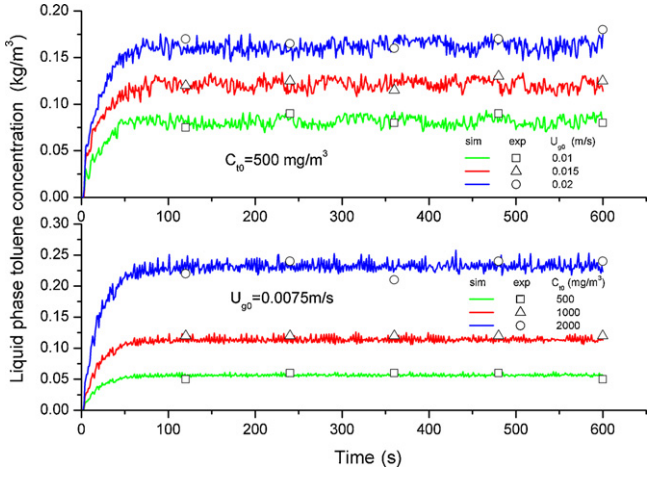

Fig. 4. Comparison of simulated and experimental DT.

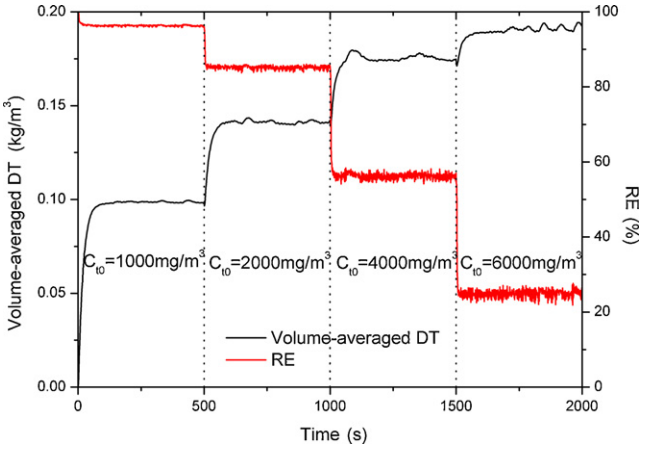

Fig. 6. Predicted shock resistance of the waste gas treating system.

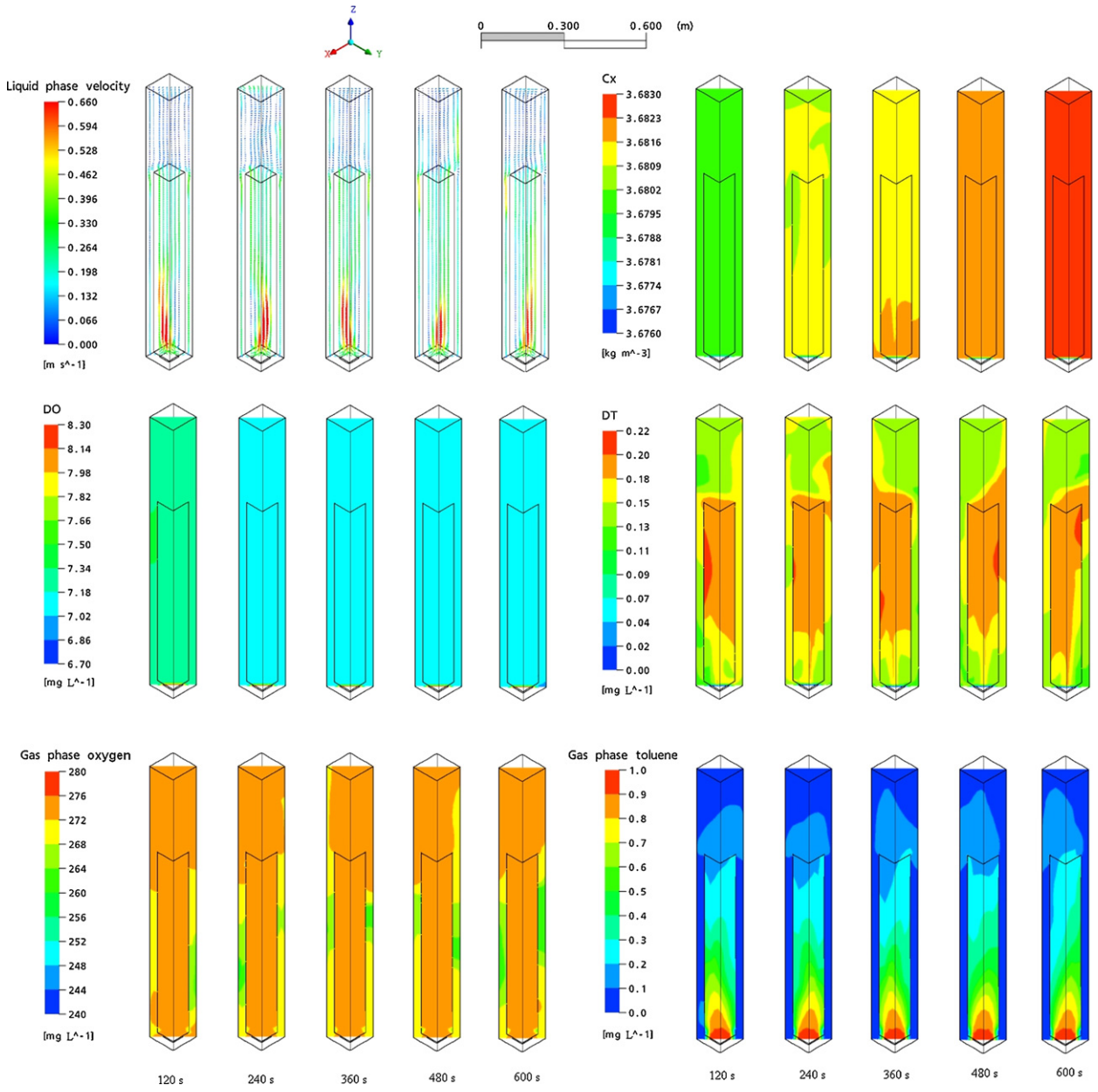

Fig. 7. Predictions of local transient variable dispersions.

described by Feng et al. [37]. The solver running over 100 s of computed time for the purification process took about 10 h on T5400 Dell Precision working station with Intel xeon inside. Convergence is good at the criteria of 1×10^{-4} for all the variables.

4. Result and discussions

4.1. Model verification

The validity of the model simulations of local axial liquid velocities was done by hydrodynamic experiments without biomass (the initial biomass concentration and toluene loading was set to be zero in simulations correspondingly), and dissolved toluene concentrations (DT) and RE were done by the waste gas treating process.

The local time-averaged axial velocities of liquid phase from simulations and LDA are compared in Fig. 3 under different superficial gas velocities (U_{g0} = 0.01, 0.015, 0.02 m/s) at various positions (x = −6 to 6 cm, y = 0, z-axis scale to diameter ratio (Z/D) = 2, 4, 6). In the draft tube, the time-averaged velocities near the central line decline with higher locations but increase as the superficial gas velocity rises for all cases. When Z/D increases, the difference of time-averaged velocities at locations on the same horizontal line in the drift tube diminishes. The liquid time-averaged axial velocity had slight increase at a fixed point when the superficial gas velocity goes up from 0.01 to 0.02 m/s. The change of height affects the liquid velocity more than the superficial gas velocity does. In the following section the local time-averaged velocities turn to the opposite direction as downward and the liquid velocity is almost stable when either the gas velocity or the geometry position changes. This is similar to the results obtained by Feng et al. [38] at Z/D = 2 and the difference at Z/D = 4, 6 can be explained that a higher Z/D value leads to a more uniform distribution of the liquid velocity. The CFD simulation results agreed well with the experiments at a deviation of 10%.

The liquid dissolved toluene (DT) concentrations were measured at the sampling point B (0, 0, 0.6 m) to verify the simulations. The quantitative comparison of the measurement and the computed results was shown in Fig. 4. Reasonable agreement was obtained through comparison of the two results with a deviation about 8%. The computed local transient DT at point B first rose up sharply in a short time period less than 100 s and then kept fluctuating around a certain value during the rest time. DT and its transient fluctuations increased with the growing toluene loading and superficial gas velocity. The fluctuations were due to turbulent flow and transient mass transfer which reflected the dynamic system.

RE is the most important variable in characterizing the treatment process and is calculated from the area-averaged gas phase toluene at the outlet surface. Transient RE is calculated from the following equation:

$$RE = \frac{C_{t0} - C_{t,out}}{C_{t0}} \times 100\% \quad (47)$$

The gas phase at the inlet and the outlet was measured for verification of the simulated transient RE in Fig. 5. When C_{t0} was 500 mg/m^3 and U_{g0} varied from 0.01 to 0.02 m/s, RE ranked from 88 to 94%. When U_{g0} was 0.0075 m/s and C_{t0} varied from 500 to 2000 mg/m^3, RE was around 93%. The experimental data had a good coincidence of 99% with the simulated results. RE went down as the superficial gas velocity increased from 0.01 to 0.02 m/s in Fig. 5a and RE changed little when the toluene loading in Fig. 5b ranged from 0.5 to 2 mg/L. Thus the superficial gas velocity affected the treatment more than the toluene loading did under the current range of operating parameters. The elimination capacity ranges from 2.9 to 11.6 mg/m^3/s calculated by the equation:

$$EC = RE \times C_{t0} \times \frac{Q_g}{V} \quad (48)$$

where Q_g is the inlet gas volume velocity and V is the working volume of the IALR.

Figs. 3–5 have showed that the proposed CFD model can well predict the fluid hydrodynamics and provide good agreement between the treatment experiment and the simulations.

4.2. Model prediction

The experimental measurements in waste gas biotreatment process are limited by the sampling positions and the design of the bioreactor such as the verification in the above section. The established CFD model can predict more information by simulation in the reactor.

Shock resistance for transient toluene loadings of the system is predicted through the simulations as toluene loading gradually increases from 1, 2, 4 to 6 mg/L with each condition simulated for 500 s. The volume-averaged DT and RE for the shock resistance were shown in Fig. 6 under U_{g0} = 0.01 m/s. The volume-averaged DT grew with the increase of C_{t0} and it took about 200 s for the volume-averaged DT to reach a new equilibrium when C_{t0} changed. RE decreased sharply when C_{t0} increased.

The local distributions of the liquid phase velocity and the local transient dispersions of DO, DT and biomass concentrations in ALR were predicted in Fig. 7 under C_{t0} = 1.0 mg/L and U_{g0} = 0.01 m/s at t = 120, 240, 360, 480 and 600 s, as well as the dispersions of toluene and oxygen in the gas phase. The liquid velocity is almost bilateral symmetry and has two circles on the central plane. The concentration of biomass increased slightly from 3.676 to 3.683 kg/m^3 during the simulation. DO at 120 s was a little higher than the rest dispersions from 240 to 600 s. The biomass concentration and DO distributed uniformly in the whole domain. DT at different time scale had no great change but the dispersions in the draft tube were always larger than those in the other sections. The dispersions of gas phase oxygen were almost the same at all time scales and the values in the following section were the lowest in the whole domain. The local toluene concentration in the gas phase decreased with the increasing height except in the following section where the gas phase toluene was uniformly small as that at the outlet.

The inner mechanism of the biotreatment process is discussed through definition of two variables, *Rolim* and *Rtlim*, the quantitative comparison of the interphase mass transfer rate and the reaction rate of oxygen and toluene, respectively:

$$Rolim = k_{lg}^{o} \frac{6}{d_g} \alpha_g (C_{o,l}^{*} - C_{o,l}) - (-r_o) \quad (49)$$

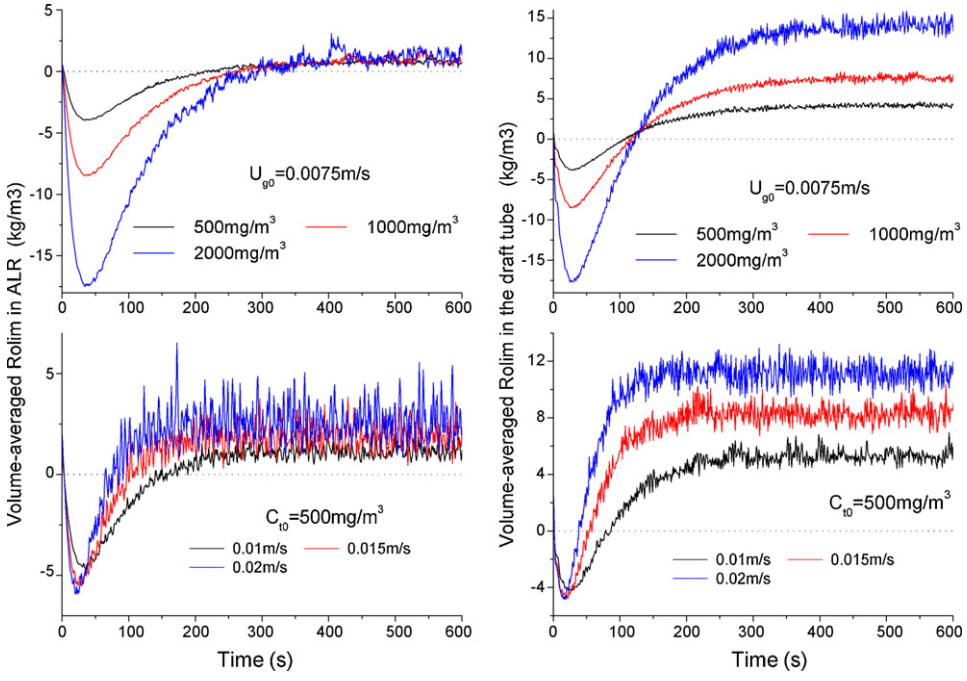

Fig. 8. Profiles of volume-averaged *Rolim* in ALR and the draft tube.

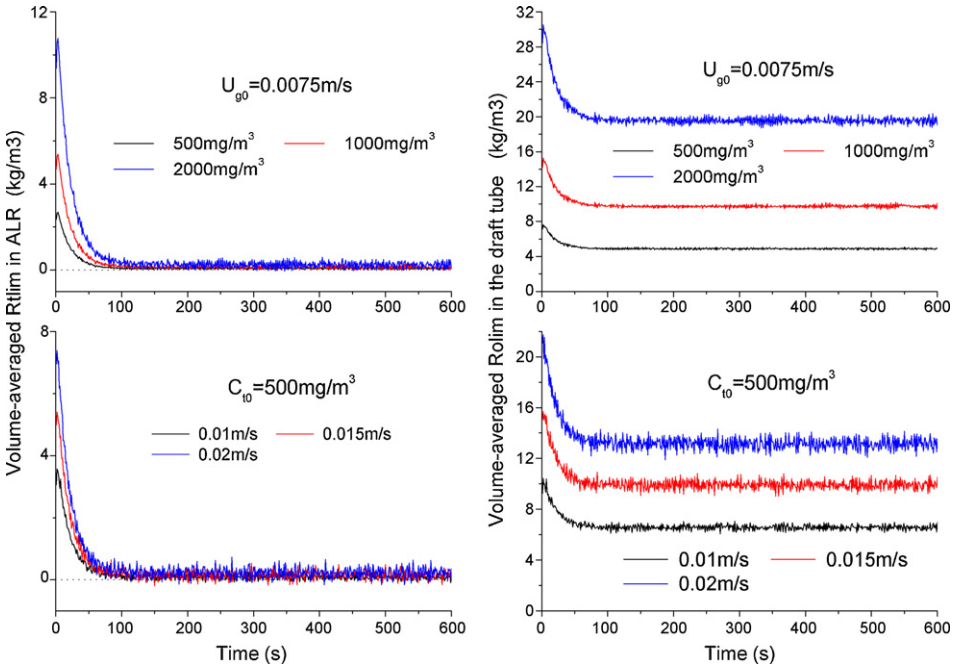

Fig. 9. Profiles of volume-averaged *Rtlim* in ALR and the draft tube.

$$Rtlim = k_{lg}^{t}\frac{6}{d_g}\alpha_g(C_{t,l}^{*} - C_{t,l}) - (-r_t) \quad (50)$$

where k_{lg}^{o}, k_{lg}^{t}, $C_{o,l}^{*}$, $C_{t,l}^{*}$, $C_{o,l}$, $C_{t,l}$, r_o and r_t are the interphase mass transfer coefficient, saturated concentration, actual concentration, the reaction rate of oxygen and toluene in the liquid phase, respectively. *Rolim* and *Rtlim* can tell the rate-limiting step in the treating process by their values.

Profiles of volume-averaged *Rolim* and *Rtlim* in IALR and in the riser tube are displayed in Figs. 8 and 9. In the whole domain *Rolim* decreases quickly first and then goes up to be slightly higher than zero while *Rtlim* declines rapidly in the first 100 s and maintains around zero in the rest computed time. Figs. 8 and 9 show that the oxygen mass transfer rate is smaller than oxygen reaction rate and the toluene mass transfer rate is larger than the toluene reaction rate in the unsteady period and then the mass transfer rate and the reaction rate are close to each other. Thus it is deduced that the limitation in the toluene waste gas treatment are the oxygen mass transfer and the toluene reaction and the oxygen mass transfer limits the treatment longer than the toluene reaction.

In the draft tube *Rolim* and *Rtlim* has the similar trend as those in the whole domain but differences also exist. *Rtlim* is always larger in the draft tube than in the whole reactor while *Rolim* in the draft tube and in the whole domain are close to each other in the first 100 s and the draft-tube-averaged *Rolim* values are larger than those in the whole domain from 100 to 600 s. This prediction discloses that the in the draft tube the toluene reaction limits the treatment all the time while for oxygen limitation changes from mass transfer to bioreaction as the process went on.

The simulation results of *RE*, *DT* and volume-averaged *Rolim* and *Rtlim* show that when biomass is in the logarithm phase and no interference is presented, the waste gas treating system rapidly goes from unsteady state to a dynamic equilibrium.

5. Conclusion

The CFD method is applied in toluene waste gas treatment process in a gas–liquid two-phase IALR and a 3D transient CFD model is established in which bioreaction, hydrodynamics and mass transfer are coupled together. The model has been validated by LDA and treatment experiments and a good agreement has been achieved. Shock resistance of the system and transient distributions of the liquid velocities and the component concentrations can be predicted. Rate-limiting steps of the treatment are also discussed. The model can be utilized to optimize the operating parameters which saves manpower. When the pollutant and biomass have changed, this model can also be applied with a new bioreaction. Provided a more precise mesh of the geometry structure, this model can be more accurate and the fluctuations of the results can be reduced. Future development of computer will make computing time less and simulate longer period of the biotreatment.

Acknowledgements

The authors wish to acknowledge the financial support provided by the National 973 Project of China (2007CB714302), International Science and Technology Cooperation Program (no. 2007DFA90530), Natural Science Foundation of Tianjin (no. 07JCZDJC01500), the National Natural Science Foundation of China (no. 20976124, no. 20906070), and Program of Introducing Talents of Discipline to Universities (no. B06006).

References

[1] J. Fenger, Air pollution in the last 50 years—from local to global, Atmos. Environ. 43 (2009) 13–22.
[2] M.F. Carvalho, A.F. Duque, S.C. Moura, C.L. Amorim, R.M. Ferreira Jorge, P.M.L. Castro, Biological treatment of a contaminated gaseous emission from a leather industry in a suspended-growth bioreactor, Chemosphere 74 (2009) 232–238.
[3] C. Kennes, F. Thalasso, Waste gas biotreatment technology, J. Chem. Technol. Biotechnol. 72 (1998) 303–319.
[4] H.H.J. Cox, M.A. Deshusses, Biological waste air treatment in biotrickling filters, Curr. Opin. Biotechnol. 9 (1998) 256–262.
[5] H.H.J. Cox, T.T. Nguyen, M.A. Deshusses, Toluene degradation in the recycle liquid of biotrickling filters for air pollution control, Appl. Microbiol. Biotechnol. 54 (1) (2000) 133–137.
[6] M.S. Vesvikar, M. Al-Dahhan, Flow pattern visualization in a mimic anaerobic digester using CFD, Biotechnol. Bioeng. 89 (2005) 719–732.
[7] S. Roy, M.T. Dhotre, J.B. Joshi, CFD simulation of flow and axial dispersion in external loop airlift reactor, Chem. Eng. Res. Des. 84 (2006) 677–690.
[8] J.M. van Baten, J. Ellenberger, R. Krishna, Hydrodynamics of internal air-lift reactors: experiments versus CFD simulations, Chem. Eng. Process 42 (2003) 733–742.

[9] J.P. Wen, Y. Chen, X.Q. Jia, D.Y. Chen, Simultaneous removal of ethyl acetate and ethanol in air streams using a gas–liquid–solid three-phase flow airlift loop bioreactor, Chem. Eng. J. 106 (2005) 171–175.
[10] A.G. Livingston, Biodegradation of 3,4-dichloroaniline in a fluidized bed bioreactor and a steady-state biofilm kinetic model, Biotechnol. Bioeng. 38 (1991) 260–272.
[11] C.S. Lo, S.J. Hwang, Dynamic behavior of an internal-loop airlift bioreactor for degradation of waste gas containing toluene, Chem. Eng. Sci. 59 (2004) 4517–4530.
[12] X.Q. Jia, J.P. Wen, X. Wang, W. Feng, Y. Jiang, CFD modeling of immobilized phenol biodegradation in three-phase airlift loop reactor, Ind. Eng. Chem. Res. 48 (2009) 4514–4529.
[13] X.Q. Jia, J.P. Wen, H.L. Zhou, Local hydrodynamics modeling of a gas–liquid–solid three-phase bubble column, AIChE J. 53 (2007) 2221–2231.
[14] M.E. Díaz, A. Iranzo, D. Cuadra, R. Barbero, F.J. Montes, M.A. Galán, Numerical simulation of the gas–liquid flow in a laboratory scale bubble column: influence of bubble size distribution and non-drag forces, Chem. Eng. J. 139 (2008) 363–379.
[15] A.A. Kulkarni, J.B. Joshi, Simultaneous measurement of flow pattern and mass transfer coefficient in bubble columns, Chem. Eng. Sci. 59 (2004) 271–281.
[16] A.A. Kulkarni, Effect of sparger design on the local flow field in a bubble column: analysis using LDA, Chem. Eng. Res. Des. 83 (2005) 59–66.
[17] R.F. Mudde, H.E.A. Van Den Akker, 2D and 3D simulations of an internal airlift loop reactor on the basis of a two-fluid model, Chem. Eng. Sci. 56 (2001) 6351–6358.
[18] J.E. Juliá, L. Hernández, S. Chiva, A. Vela, Hydrodynamic characterization of a needle sparger rectangular bubble column: homogeneous flow, static bubble plume and oscillating bubble plume, Chem. Eng. Sci. 62 (2007) 6361–6377.
[19] R.F. Mudde, J.S. Groen, H.E.A. Van Den Akker, Liquid velocity field in a bubble column: LDA experiments, Chem. Eng. Sci. 52 (1997) 4217–4224.
[20] J.S. Groen, R.F. Mudde, H.E.A. Van Den Akker, On the application of LDA to bubbly flow in the wobbling regime, Exp. Fluids 27 (1999) 435–449.
[21] M. Simonnet, C. Gentric, E. Olmos, N. Midoux, CFD simulation of the flow field in a bubble column reactor: importance of the drag force formulation to describe regime transitions, Chem. Eng. Process 47 (2008) 1726–1737.
[22] S.S. Thakre, J.B. Joshi, CFD simulation of bubble column reactors: importance of drag force formulation, Chem. Eng. Sci. 54 (1999) 5055–5060.
[23] M. Ishii, N. Zuber, Drag coefficient and relative velocity in bubbly, droplet or particulate flows, AIChE J. 25 (1979) 843–855.
[24] D. Lucas, H.-M. Prasser, A. Manera, Influence of the lift force on the stability of a bubble column, Chem. Eng. Sci. 60 (2005) 3609–3619.
[25] M.V. Tabib, S.A. Roy, J.B. Joshi, CFD simulation of bubble column—an analysis of interphase forces and turbulence models, Chem. Eng. J. 139 (2008) 589–614.
[26] M. Simcik, M.C. Ruzicka, J. Drahoš, Computing the added mass of dispersed particles, Chem. Eng. Sci. 63 (2008) 4580–4595.
[27] D. Zhang, N.G. Deen, J.A.M. Kuipers, Numerical simulation of the dynamic flow behavior in a bubble column: a study of closures for turbulence and interface forces, Chem. Eng. Sci. 61 (2006) 7593–7608.
[28] M. Lopez de Bertodano, Turbulent bubbly two-phase flow in a triangular, Duct, PhD thesis, Renssealaer Polytechnic Institute, Troy, New York, 1991.
[29] F.J. Moraga, A.E. Larreteguy, D.A. Drew, R.T. Lahey Jr., Assessment of turbulent dispersion models for bubbly flows in the low Stokes number limit, Int. J. Multiphase Flow 29 (2003) 655–673.
[30] H.A. Jakobsen, B.H. Sannes, S. Grevskott, H.F. Svendsen, Modeling of vertical bubble-driven flows, Ind. Eng. Chem. Res. 36 (1997) 4052–4074.
[31] Y. Sato, K. Sekoguchi, Liquid velocity distribution in two-phase bubbly flow, Int. J. Multiphase Flow 2 (1975) 79–95.
[32] B.E. Launder, D.B. Spalding, The numerical computation of turbulent flows, Comput. Methods Appl. Mech. Eng. 3 (1974) 269–289.
[33] H. Luo, H. Svendsen, Theoretical model for drop and bubble breakup in turbulent dispersions, AIChE J. 42 (1996) 1225–1233.
[34] M. Prince, H. Blanch, Bubble coalescence and break-up in air-sparged bubble columns, AIChE J. 36 (1990) 1485–1499.
[35] J.E. Bailey, D.F. Ollis (Eds.), Biochemical Engineering Fundamentals, McGraw-Hill, New York, NY, USA, 1986.
[36] P. Chen, M.P. Dudukovic, J. Sanyal, Three-dimensional simulation of bubble column flows with bubble coalescence and breakup, AIChE J. 51 (2005) 696–712.
[37] W. Feng, J.P. Wen, J.H. Fan, Q. Yuan, X.Q. Jia, Y. Sun, Local hydrodynamics of gas–liquid-nanoparticles three-phase fluidization, Chem. Eng. Sci. 60 (2005) 6887–6898.
[38] W. Feng, J.P. Wen, C.Y. Liu, Q. Yuan, X.Q. Jia, Y. Sun, Modeling of local dynamic behavior of phenol degradation in an internal loop airlift bioreactor by yeast *Candida tropicalis*, Biotechnol. Bioeng. 97 (2007) 251–264.